Non-uniform programmable photonic waveguide meshes

Supplementary Notes

Cristina Catalá-Lahoz[1*] and Jose Capmany[1*]

[1*]Photonics Research Labs, iTEAM Research Institute, Universitat Politècnica de València, Camí de vera s/n, Valencia, 46022, Valencia, Spain.

*Corresponding author(s). E-mail(s): ccatala@iteam.upv.es; jcapmany@iteam.upv.es;

Contents

Supplementary Note 1. Modelling and optimization of the Vernier effect

A serially coupled double-ring resonator enables the extension of the free spectral range (FSR) to the least common multiple of the FSR of the individual rings [1]. This is achieved by designing the two rings with different radii. When light propagates through the double-ring resonator, it is transmitted from the drop port only when both rings meet their respective resonance conditions. The resulting FSR of the double-ring resonator with distinct radii can be expressed as:

$$\text{FSR}_\text{T} = n\text{FSR}_1 = m\text{FSR}_2 \tag{1}$$

Multiplying both sides of the first by FSR_2 and both sides of the second by FSR_1, we get:

$$\text{FSR}_\text{T}\text{FSR}_2 = n\text{FSR}_1\text{FSR}_2 \tag{2}$$

$$\text{FSR}_\text{T}\text{FSR}_1 = m\text{FSR}_2\text{FSR}_1 \tag{3}$$

Then, we subtract both equations to get:

$$\text{FSR}_\text{T} \cdot |\text{FSR}_1 - \text{FSR}_2| = |m - n| \cdot \text{FSR}_1\text{FSR}_2 \tag{4}$$

Which leads to:

$$\text{FSR}_\text{T} = |m - n|\frac{\text{FSR}_1 \cdot \text{FSR}_2}{|\text{FSR}_1 - \text{FSR}_2|} \tag{5}$$

Where n and m are natural and coprime numbers, so $|m - n| = 1$:

$$\text{FSR}_\text{T} = \frac{\text{FSR}_1 \cdot \text{FSR}_2}{|\text{FSR}_1 - \text{FSR}_2|} \tag{6}$$

The schematic of a serially coupled double-ring resonator is depicted in Fig. 1. From this model, the fields can be calculated as follows:

$$E_{1a} = -\kappa_1^* E_i + t_1^* \alpha_1 e^{j\omega \frac{\tau_1}{2}} E_{1b} \tag{7}$$

$$E_{1b} = t_2^* \alpha_1 e^{j\omega \frac{\tau_1}{2}} E_{1a} - \kappa_2^* \alpha_2 e^{j\omega \frac{\tau_2}{2}} E_{2b} \tag{8}$$

$$E_{2a} = \kappa_2 \alpha_1 e^{j\omega \frac{\tau_1}{2}} E_{1a} + t_2 \alpha_2 e^{j\omega \frac{\tau_2}{2}} E_{2b} \tag{9}$$

$$E_{2b} = -\kappa_3^* E_a + t_3^* \alpha_2 e^{j\omega \frac{\tau_2}{2}} E_{2a} \tag{10}$$

$$E_t = t_1 E_i + \kappa_1 \alpha_1 e^{j\omega \frac{\tau_1}{2}} E_{1b} \tag{11}$$

$$E_d = t_3 E_a + \kappa_3 \alpha_2 e^{j\omega \frac{\tau_2}{2}} E_{2a} \tag{12}$$

Where $\alpha_1 = \alpha_{\text{R1}/2}$ and $\alpha_2 = \alpha_{\text{R2}/2}$ represent the loss coefficients of the half round-trip length of the rings, $\omega = 2\pi f$ is the frequency vector, and $\tau = L/c$ is the round trip delay. From (7) to (12), the general expressions for the transfer functions for the throughput and the drop port can be derived. Here we assume a coupler without losses and symmetric coupling behaviour, so $t = t^*$ and $\kappa = \kappa^*$ (note that $|t^2| + |\kappa^2| = 1$). Assuming that there is no input field in the add port ($E_a = 0$), we obtain:
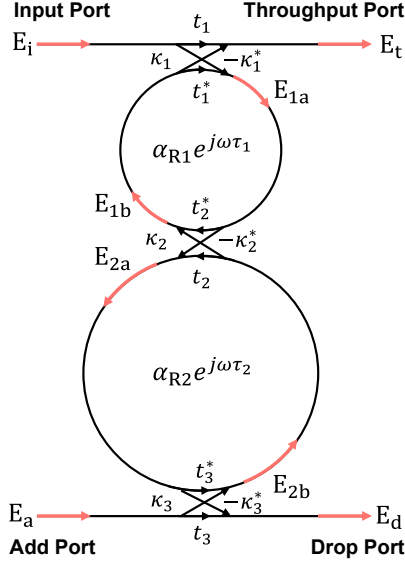
2

Fig. 1 Serially coupled double-ring resonator

$$\frac{E_t}{E_i} = \frac{-t_1\kappa_1^2\alpha_1^2 e^{j\omega\tau_1}(t_3\alpha_2^2 e^{j\omega\tau_2} - t_2)}{1 - t_1 t_2\alpha_1^2 e^{j\omega\tau_1} - t_2 t_3\alpha_2^2 e^{j\omega\tau_2} + t_1 t_3\alpha_1^2\alpha_2^2 e^{j\omega\tau_1} e^{j\omega\tau_2}} \tag{13}$$

$$\frac{E_d}{E_i} = \frac{\kappa_1\kappa_2\kappa_3\alpha_1\alpha_1 e^{j\frac{\omega\tau_1}{2}} e^{j\frac{\omega\tau_2}{2}}}{1 - t_1 t_2\alpha_1^2 e^{j\omega\tau_1} - t_2 t_3\alpha_2^2 e^{j\omega\tau_2} + t_1 t_3\alpha_1^2\alpha_2^2 e^{j\omega\tau_1} e^{j\omega\tau_2}} \tag{14}$$

47

48 If we have a serially coupled structure of N rings, where each ring has a different
49 length and therefore a different FSR, we could deduce its total FSR recursively:

$$\text{FSR}_{\text{T}_1} = \frac{\text{FSR}_1 \cdot \text{FSR}_2}{|\text{FSR}_1 - \text{FSR}_2|} \tag{15}$$

$$\text{FSR}_{\text{T}_2} = \frac{\text{FSR}_{\text{T}_1} \cdot \text{FSR}_3}{|\text{FSR}_{\text{T}_1} - \text{FSR}_3|} = \frac{\text{FSR}_1 \cdot \text{FSR}_2 \cdot \text{FSR}_3}{|\text{FSR}_1 - \text{FSR}_2| \cdot \left| \frac{\text{FSR}_1 \cdot \text{FSR}_2}{|\text{FSR}_1 - \text{FSR}_2|} - \text{FSR}_3 \right|} \tag{16}$$

50 This brings us to the following equation for structures with $N > 2$:

$$\text{FSR}_{\text{T}_N} = \text{FSR}_{\text{T}_1} \cdot \prod_{i=3}^{N} \frac{\text{FSR}_i}{\left| \text{FSR}_i - \text{FSR}_{\text{T}_{i-2}} \right|} \tag{17}$$

3

Supplementary Note 2. Introducing defect cells in hexagonal meshes

In a programmable photonic mesh, it is possible to introduce defects or non-uniformities in different ways, allowing for controlled modifications to the structure and functionality of the system [2]. Below, we will describe two specific cases where the overall hexagonal perimeter of the mesh is preserved. In the first case, we introduce one or multiple Mach-Zehnder Interferometers (MZIs) inside the hexagons. In the second case, we shorten one of the hexagonal sides.

The first case is the one discussed in this work, where a defect MZI is introduced inside the hexagonal cell. Figure 2a shows an example of possible configurations (note that more combinations are possible). The first defect, shown in red in the left-most panel, represents a horizontal modification within the mesh. The second defect, highlighted in purple in the second panel, introduces modification with two different cavities inside the hexagonal cell. Finally, the third defect depicted in blue, forms a vertical variation with three cavities inside the cell, using two MZIs.
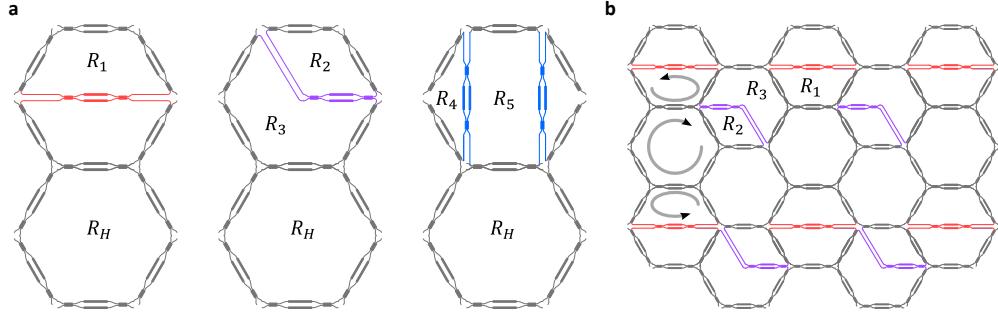

Fig. 2 (a) Different configurations of defect cells introduced into a hexagonal mesh. The defects modify the internal structure while maintaining the external hexagonal perimeter. (b) Example of a scalable non-uniform programmable mesh with strategically placed defects.

These defects can be distributed within the programmable hexagonal framework. Figure 2b shows an example of how we can scale a programmable mesh with defects. The modifications are applied in alternating rows to create a structured non-uniformity, where all the cavities can be connected with the hexagonal one.

Figure 3a represents another configuration of a non-uniform programmable photonic mesh, where specific modifications are introduced to alter the structure and optical behaviour of the hexagonal network. A single hexagonal unit is shown with local changes. The red-highlighted elements indicate the introduction of Mach-Zehnder Interferometers (MZIs) along the side edges of the hexagon, with a shorter length, forming an extension of the hexagon itself.

Figure 3b shows a larger section of the photonic mesh, where these modifications are systematically arranged. The defect cells are distributed in columns, creating a periodic pattern that introduces non-uniformities in the structure.
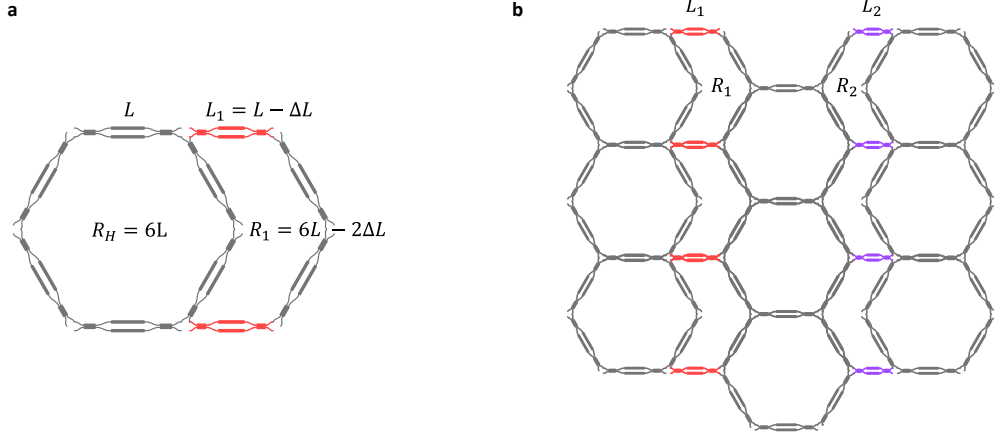
Fig. 3 (a) A hexagonal cell with a defect cell placed in series. (b) Large-scale implementation of the defect-cell approach, showing periodic non-uniformities across the structure in columns.

One of the problems with adding the defect as shown in Fig. 3 is that we waste one of the connections of the hexagons adjacent to the defect cells. Therefore, one way to solve this would be to follow this structure but keep the connections of the original uniform mesh (Fig. 4a). In this case, we must also introduce the defect cells in columns as shown in Fig. 4b.
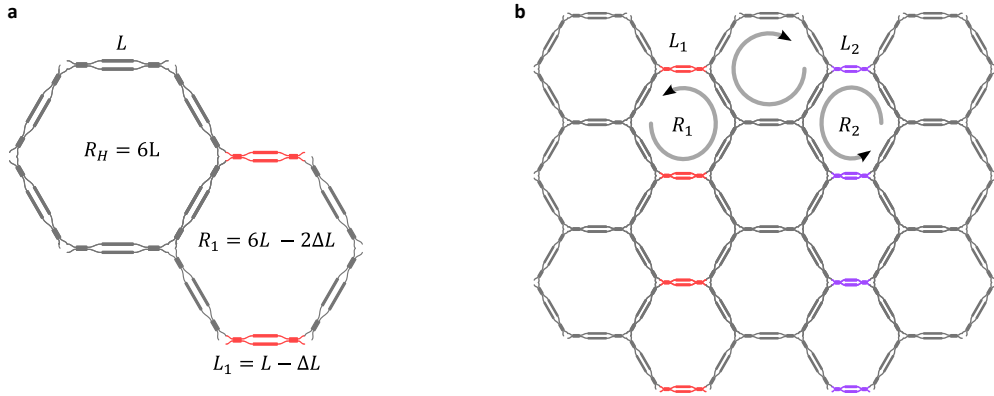

Fig. 4 (a) Alternative defect-cell configuration preserving original uniform mesh connections. (b) Column-based distribution of defect cells to maintain connectivity while introducing structured non-uniformities.

Supplementary Note 3. Flattened hexagonal mesh design

For the design of the layout of the fabricated chip, the available space was limited and therefore, the hexagonal cells have been modified so that they take up less space on one of the axes. To do this, the hexagonal shape has been "flattened", making all the MZI positioned at the same angle [3]. Figure 5 shows the three cell designs presented in this work in their flatten-like form.

In this type of configuration, it is necessary to add an extra length to each side of the MZI to make the joints between them. This makes the length of each side of the hexagon Ls, inevitably a little longer than in the traditional hexagonal design. In the case of defects, it has been necessary to adjust the lengths by adding extra paths or spirals, to obtain the required roundtrip of the ring to create the Vernier effect. The
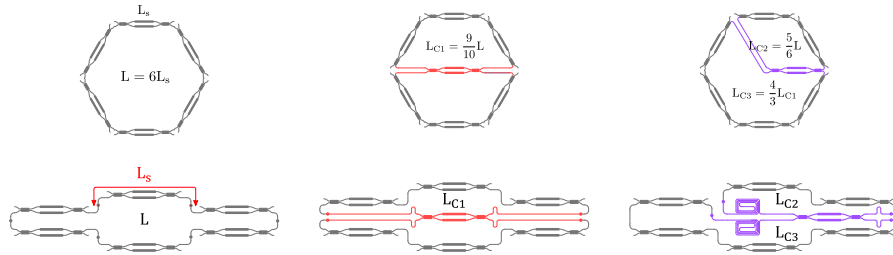

Fig. 5 Flattened hexagonal mesh designs optimized for space efficiency. The modified layout aligns all MZIs at the same angle, minimizing footprint while maintaining functionality.

complete layout of the non-uniform mesh is shown in Fig. 6, including edge couplers, DC pads and metal tracks. The MZIs in the default cells are highlighted in red and purple.
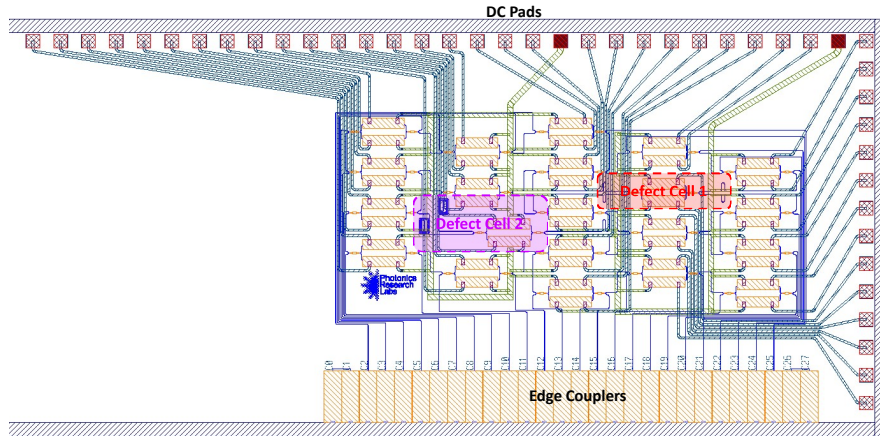

Fig. 6 Complete layout of the non-uniform programmable photonic mesh, including edge couplers, DC pads, and metal tracks. MZIs in the defect cells are highlighted in red and purple.

6

Supplementary Note 4. Characterization and calibration of the device

The characterization of the MZI of the mesh was carried out manually since in this case, it is a small mesh. Other calibrations based on graphs can be used for automatic calibration [4, 5]. In this case, we have used a fixed laser at 1550 nm and a power meter to measure the optical power at the output. First, a characterization of the MZIs that are in the perimeter of the mesh has been carried out, since having only 2 of 4 ports connected, their characterization is simpler. To do this, we have followed a recirculating characterization scheme. Fig. 7 shows 3 examples of MZI that are located on the perimeter of the hexagonal cell on the left, with the MZI to be characterized in blue and the optical path followed in red. By recirculating scheme, we imply that
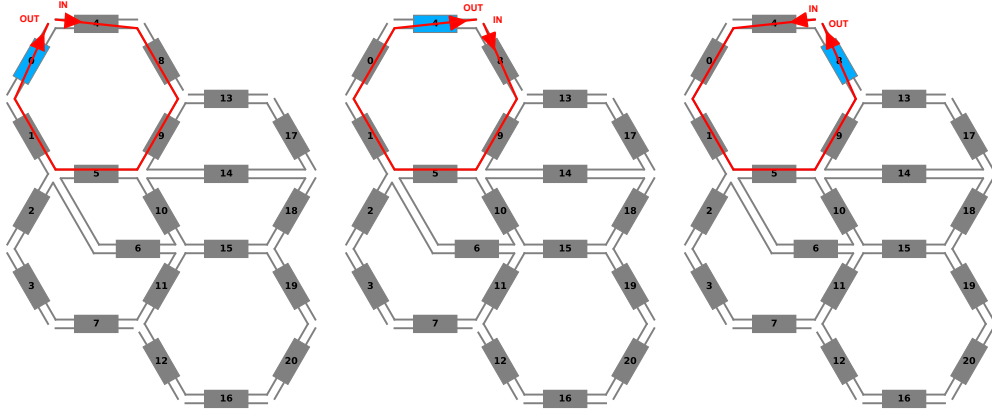

Fig. 7 Examples of configurations for MZI characterization in the perimeter of the hexagonal mesh. The optical paths used for characterization are highlighted in red.

we use as an output port the MZI that we want to characterize and any input port that has direct access to the cell where that MZI is located. Assuming that enough light reaches the MZI that we are characterizing, we sweep each of its phase shifters in current and measure the optical power at the output. With this, we will have characterized the MZI without any interfering signal on the other input port.

Once the MZIs from the perimeter of the mesh have been characterized, we can characterize the inner MZIs by following the same technique and putting the adjacent MZI in a *cross* state so that it interferes.

The MZI are implemented by using two 3-dB couplers, where each arm incorporates a tunable phase shifter as shown in Fig. 8. Considering MMIs for the 3-dB couplers
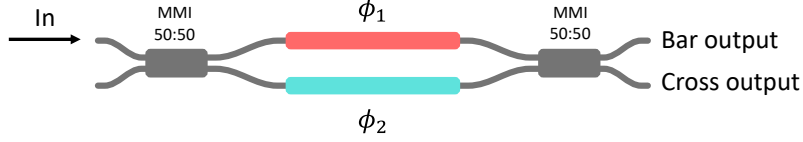
Fig. 8 Schematic representation of an MZI implementation using two 3-dB couplers, with tunable phase shifters for independent control of phase and coupling.

[6], the transmission matrix results in:

$$
\begin{aligned}
T &= \frac{je^{j\varphi_0}}{\sqrt{2}}\frac{je^{j\varphi_0}}{\sqrt{2}}\begin{pmatrix} 1 & j \\ j & 1 \end{pmatrix}\begin{pmatrix} e^{-j\phi_1} & 0 \\ 0 & e^{-j\phi_2} \end{pmatrix}\begin{pmatrix} 1 & j \\ j & 1 \end{pmatrix} = \\
&= \frac{e^{j(2\varphi_0+\pi)}}{2}\begin{pmatrix} 1 & j \\ j & 1 \end{pmatrix}\begin{pmatrix} e^{-j\phi_1} & je^{-j\phi_1} \\ je^{-j\phi_2} & e^{-j\phi_2} \end{pmatrix} = \\
&= \frac{e^{j(2\varphi_0+\pi)}}{2}\begin{pmatrix} e^{-j\phi_1}-e^{-j\phi_2} & je^{-j\phi_1}+je^{-j\phi_2} \\ je^{-j\phi_1}+je^{-j\phi_2} & -e^{-j\phi_1}+e^{-j\phi_2} \end{pmatrix} = \\
&= e^{j\left(2\varphi_0-\frac{\phi_1+\phi_2-3\pi}{2}\right)}\begin{pmatrix} \sin\left(\frac{\phi_2-\phi_1}{2}\right) & \cos\left(\frac{\phi_2-\phi_1}{2}\right) \\ \cos\left(\frac{\phi_2-\phi_1}{2}\right) & -\sin\left(\frac{\phi_2-\phi_1}{2}\right) \end{pmatrix},
\end{aligned}
\tag{18}
$$

where $\varphi_0 = -\beta_0 L_{\mathrm{MMI}} - 3\pi/4$ is the phase corresponding to the 2×2 MMIs.

We can define the final transfer matrix, considering the overall phase and coupling as follows:

$$
\varphi = -\frac{\phi_1+\phi_2}{2}
\tag{19}
$$

$$
\theta = \frac{\phi_2-\phi_1}{2}
\tag{20}
$$

Which leads to:

$$
T = -je^{j\varphi}\begin{pmatrix} \sin\theta & \cos\theta \\ \cos\theta & -\sin\theta \end{pmatrix},
\tag{21}
$$

Equation (18) represents a tunable coupler where the coupling constant $\kappa = \cos^2\theta$ and the overall phase shift φ can be independently tuned according to the system of two equations given by (16) and (17).

For example, for implementing a tunable ring resonator in the mesh, an example in Fig.9 is shown. Here we use phase shifter 16 for coupling the light to the ring with a coupling factor κ driving only one of the phase shifters of that MZI. Currents of the MZIs 11, 12, 15, 19 and 20 are set to provide a coupling factor $\kappa = 1.0$ (i.e., bar state). Blue MZIs are also controlled using only one phase shifter. Then, MZI number 19 (depicted in orange) is set using both phase shifters. In that way, we can maintain the bar state and also tune the phase of the ring. To do that, we set the current i_0 of one of the phase shifters (ϕ_1 for example) for having the coupling $\kappa = 1.0$ and then we can tune the phase of the ring changing the current of the two phase shifters as following:

$$
i_1 = \sqrt{i_0^2 + i_r^2}
\tag{22}
$$

8

$$i_2 = i_r, \tag{23}$$

where i_1 and i_2 are the current of each phase shifter and i_r the additional current to control the phase. Figure 10 shows the measurement of a characterized MZI, where
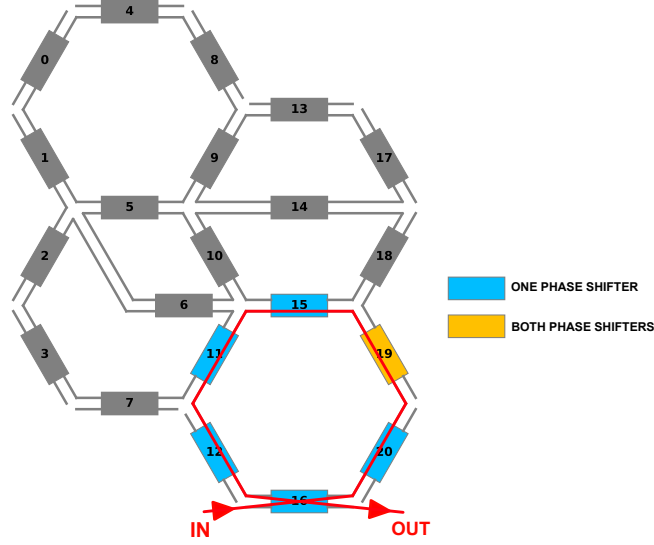

Fig. 9 Example of a tunable ring resonator implemented within the programmable mesh. Specific MZIs are controlled to define the coupling factor and phase tuning.

coupling can be observed as a function of current (left side) and also the measurement
in dB as a function of the power applied to the phase shifter (right side). In addition,
the fitting performed using the above equations can be observed, where $\theta = p_0 +$
$p_1 I + p_2 I^2 + p_3 I^3 + p_4 I^4$. Higher orders than I^2 were used to take into consideration
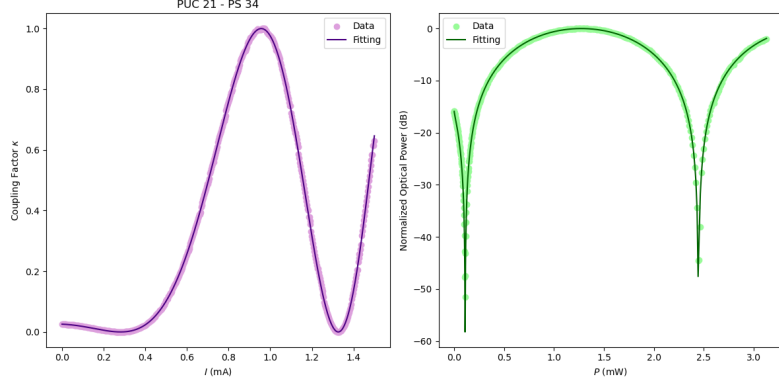fabrication deviations.

Fig. 10 Measured coupling as a function of applied current (left) and transmission response in dB (right). The experimental data is fitted using a polynomial model to account for fabrication deviations.

Supplementary Note 5. Setup preparation and measurement

For optical spectral measurements, we used a tunable laser source (T100S-HP EXFO) along with a component tester (CT440 EXFO), featuring a 1 pm wavelength resolution. Figure 11 shows in more detail the optical connections between the different equipment. Active optical alignment was performed automatically using piezo con-
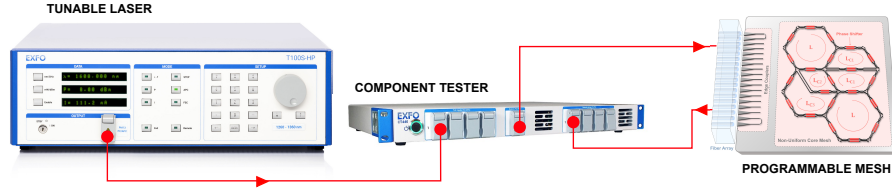

Fig. 11 Experimental setup for optical spectral measurements, including a tunable laser source, component tester, and programmable photonic mesh.

trollers (Thorlabs MDT693B) for the positioner that held the fibre array. The alignment routine consists of finding, simultaneously, high optical output power at both loops of the edge coupler array. A 7 dB loss is measured for the loop ports, corresponding to a 3.5 dB loss per input, including the coupling and insertion losses of the edge couplers.

The 42 DC channels are wirebonded to a printed circuit board (PCB) and controlled with a multichannel current source (Qontrol Ltd.) that can be programmed through coding.

To have a stable temperature during measurements, we use a temperature controller (Thorlabs TED200C) along with a Peltier cooler and a thermistor. A heatsink

10

was placed under the whole packaged device for heat dissipation as shown in Fig. 12, with a more detailed view of all the components.
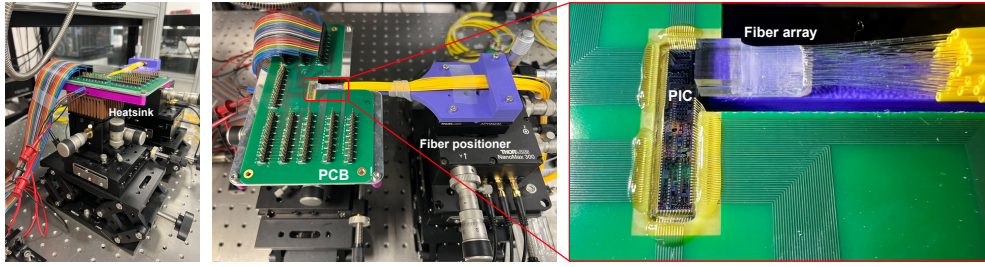

Fig. 12 Setup for thermal stabilization during measurements, featuring a temperature controller, Peltier cooler, fiber positioner, and printed circuit board (PCB).

Supplementary Note 6. Characterization of the different cells

Once the entire mesh was characterized, each of the designed cavities was characterized separately by programming simple rings with a random coupling. In Fig. 13 you can see the spectral measurement of each of these cavities, using the setup in Fig. 11.

In Fig. 13a, the FSR of the L_{C2} ring is compared with the L_{C3} ring, seeing how their resonances coincide with every 4 FSRs of the L_{C3} cavity. Figure 13b,c shows the measurements for the L_{C2} and L_{C1} cavities compared to the hexagonal cavity, showing the resonances that coincide every 6 and 10 FSRs, respectively. Therefore, this is a preliminary way of verifying that it is possible to observe the Vernier effect demonstrated in this work, by coupling each pair of these cavities.
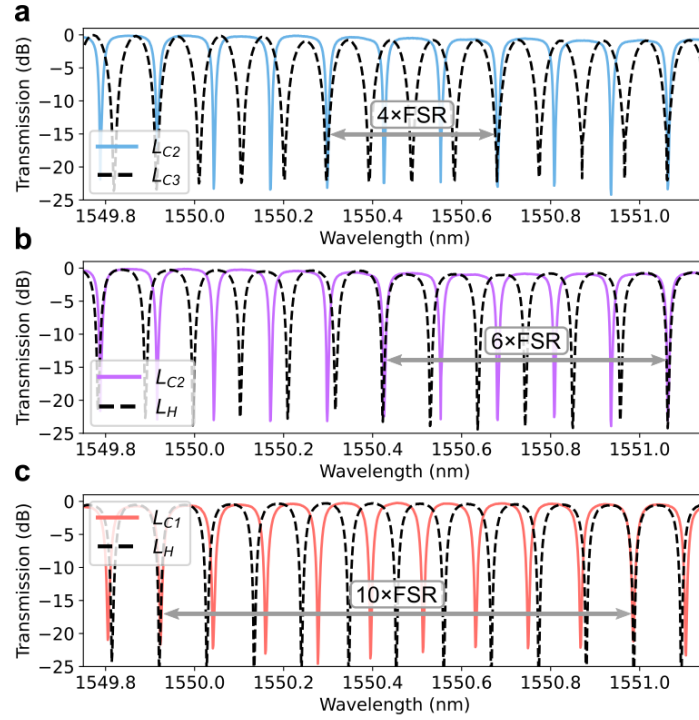

Fig. 13 Spectral measurements of individual cavities within the programmable mesh, verifying the feasibility of the Vernier effect by comparing resonances of different-sized cavities.

Supplementary Note 7. Kramers-Kronig relations for phase response

The Kramers-Kronig relations establish a fundamental connection between the real and imaginary parts of a complex function that is analytic in the upper half-plane [7]. The fundamental principle behind these relations is causality: the response of a system at a given time depends only on past interactions. This constraint imposes mathematical relationships between different components of a function in the frequency domain, allowing one part to be determined if the other is known.

For a causal response function $H(\omega)$, the real and imaginary components are related via the Hilbert transform:

$$\text{Re}[H(\omega)] = \frac{1}{\pi}\mathcal{P}\int_{-\infty}^{\infty}\frac{\text{Im}[H(\omega')]}{\omega'-\omega}d\omega', \tag{24}$$

$$\text{Im}[H(\omega)] = -\frac{1}{\pi}\mathcal{P}\int_{-\infty}^{\infty}\frac{\text{Re}[H(\omega')]}{\omega'-\omega}d\omega', \tag{25}$$

where $\mathcal{P}$ denotes the Cauchy principal value. These integrals ensure that if one part of the function is known over all frequencies, the other can be uniquely determined, provided the function satisfies the necessary analyticity and decay conditions.

If we consider a complex function of frequency $H(\omega) = A(\omega)e^{i\phi(\omega)}$, where $A(\omega)$ is the amplitude and $\phi(\omega)$ is the phase, the phase can be directly obtained from the amplitude using:

$$\phi(\omega) = \frac{2\omega}{\pi}\mathcal{P}\int_{0}^{\infty}\frac{\ln A(\omega')}{\omega'^2-\omega^2}d\omega'. \tag{26}$$

This relation allows phase reconstruction from measured amplitude spectra. The practical application of these relations requires numerical techniques for evaluating the principal value integral. Common approaches include Fourier-based Hilbert transforms and discrete numerical integration methods.

Supplementary References

[1] Rabus, D. *Integrated Ring Resonators: The Compendium* Springer Series in Optical Sciences (Springer Berlin Heidelberg, 2007).

[2] Catalá-Lahoz, C. & Capmany, J. *Non-uniform programmable integrated photonic waveguide hexagonal mesh*, 1–2 (2024).

[3] López, D. P. Programmable integrated silicon photonics waveguide meshes: Optimized designs and control algorithms. *IEEE Journal of Selected Topics in Quantum Electronics* **26**, 1–12 (2020).

[4] Pérez-López, D., López, A., DasMahapatra, P. & Capmany, J. Multipurpose self-configuration of programmable photonic circuits. *Nature Communications* **11**, 1–11 (2020).

[5] López-Hernández, A., Gutiérrez-Zubillaga, M. & Pérez-López, D. *Automatic self-calibration of programmable photonic processors*, 1–2 (2022).

[6] Capmany, J. & Pérez, D. *Programmable Integrated Photonics* (Oxford University Press, New York, 2020).

[7] Lucarini, V., Saarinen, J., Peiponen, K. & Vartiainen, E. *Kramers-Kronig Relations in Optical Materials Research* Springer Series in Optical Sciences (Springer Berlin Heidelberg, Berlin, 2005).